



# Magnetic Effects on Microstructure and Solute Plume Dynamics of Directionally Solidifying Ga-In Alloy

ANDREW KAO <sup>1,5</sup> NATALIA SHEVCHENKO,<sup>2</sup> SHENGYA HE,<sup>2,3</sup>  
PETER D. LEE <sup>4</sup> SVEN ECKERT,<sup>2</sup> and KOULIS PERICLEOUS <sup>1</sup>

1.—Centre for Numerical Modelling and Process Analysis, Old Royal Naval College, University of Greenwich, Park Row, London SE109LS, UK. 2.—Helmholtz-Zentrum Dresden-Rossendorf, Institute of Fluid Dynamics, Bautzner Landstrasse 400, 01328 Dresden, Germany. 3.—State Key Laboratory of Advanced Special Steel & School of Materials Science and Engineering, Shanghai University, Shanghai 200444, People's Republic of China. 4.—Mechanical Engineering, University College London, London WC1E 6BT, UK. 5.—e-mail: a.kao@greenwich.ac.uk

The effects of applying a 0.2-T transverse magnetic field on a solidifying Ga-25 wt%In alloy have been investigated through a joint experimental and numerical study. The magnetic field introduced significant changes to both the microstructure and the dynamics of escaping high-concentration Ga plumes. Plume migration across the interface was quantified and correlated to simulations to demonstrate that thermoelectric magnetohydrodynamics (TEMHD) is the underlying mechanism. TEMHD introduced macrosegregation within the dendritic structure, leading to the formation of a stable “chimney” channel by increasing the solutal buoyancy in the flow direction. The resulting pressure difference across the solidification front introduced a secondary hydrodynamic phenomenon that subsequently caused solute plume migration.

## INTRODUCTION

During solidification of alloys, partitioning of elements leads to the formation of a solute boundary layer in the vicinity of the liquid–solid interface. This paper considers the behavior of alloys, such as industrial nickel-based superalloys, where the density of the solute may be lighter than that of the bulk liquid. This leads to strong buoyancy forces in this solute layer directed back towards the bulk liquid, causing the formation of solute plumes that emanate from the interface. Under certain conditions, the escaping solute can form stable channels, or chimneys, that when fully solidified become a defect known as “freckles”.<sup>1–4</sup> The aim of this work is to investigate the effects of applying a magnetic field on such systems, with the long-term goal of

using magnetic fields to tailor the microstructure and control the solute segregation so as to enhance the properties of cast components.

During solidification, inherent thermoelectric currents are formed due to the variation in composition by phase and thermal gradient. These currents interact with an externally applied magnetic field, generating a thermoelectric Lorentz force (TEF) that drives flow through a phenomenon known as thermoelectric magnetohydrodynamics (TEMHD). The TEMHD effect, also known as thermoelectric magnetic convection (TEMC), has been shown to introduce many changes to the microstructure, including macrosegregation<sup>5–7</sup> that leads to a tilted interface,<sup>8</sup> the formation of solute pockets,<sup>6,9</sup> banded structures,<sup>10</sup> modification to the primary arm spacing,<sup>11</sup> and the formation of stray grains in single-crystal castings.<sup>12</sup> Most of the cited studies were carried out on alloys where the solute density was higher than in the bulk liquid, hence solute plumes do not spring from the interface; however, similar changes are also observed in systems where the solute is the lighter element.<sup>11–13</sup> Most of these studies use *post mortem* analysis of the final

(Received May 22, 2020; accepted July 22, 2020)

solidified structures to investigate the changes in order to understand the associated mechanisms. Dynamic *in situ* observations can provide further insights into the underlying physics of the process; for example, in previous work, the authors investigated the formation of large-scale channels through a joint experimental and numerical approach, using the analogous Ga-25 wt%In system.<sup>14</sup> The current investigation uses a similar approach, but with the addition of a transverse external magnetic field to both the experiment and the numerical predictions.

## EXPERIMENTAL SETUP

*In situ* solidification experiments were performed at the Helmholtz-Zentrum Dresden-Rossendorf (HZDR). The solidification setup had already been employed in previous radiographic investigations carried out by means of a microfocus X-ray tube and is described in detail elsewhere.<sup>15,16</sup>

The nominal composition of the Ga-25 wt%In alloy was prepared from 99.99% Ga and 99.99% In. The alloy was melted and filled into a windowed Hele–Shaw cell with liquid metal dimensions of 30 mm × 30 mm × 0.15 mm (Fig. 1a).

A transverse direct-current (DC) magnetic field was generated by two ring-shaped permanent magnets (Nd–Fe–B) with internal intensity of 1.17 T. The inner diameter of the magnet was 10 mm, the outer diameter was 18 mm, and the thickness was 5 mm. An iron core was designed to constrain the magnetic flux to the sample volume. The magnets were fixed onto the iron core and the sample was placed in between, as shown in Fig. 1b. The magnetic field intensity measured by means of a Gauss meter was found to be reasonably homogeneous, varying from 0.18 T at the outer edge of the magnetic system to 0.26 T between the ring magnets and 0.19 T in the center. More details of the magnetic system can be found in Ref. 17. A COMSOL Multiphysics V5.2 simulation shows that the direction of the magnetic field is perpendicular to the sample surface, as displayed in Fig. 1c.

The heating/cooling system contained two sets of Peltier units which were in thermal contact with the top and bottom edges of the solidification cell. The synchronized regulation of the power of both Peltier elements, by means of a proportional–integral–derivative (PID) controller unit, allowed for the adjustment of the cooling rate and the temperature gradient during the process. The distance between the heater and the cooler was  $\sim 23$  mm. The temperature difference  $\Delta T$  between the heater and the cooler was measured using two miniature K-type thermocouples in thermal contact with the outer surface of the cell near the edge of the Peltier elements. The accuracy of the temperature control was  $\pm 0.3$  K. The samples were directionally solidified from bottom to top using a temperature gradient of 2 K/mm and cooling rates of 0.01 K/s or 0.005 K/s.

The solidification setup was mounted on a three-axis translation stage between a microfocus X-ray source (XS225D-OEM, Phoenix X-ray, Germany) and an X-ray detector (TH9438HX 9", Thales, France). The configuration of the ring magnets, which mask part of the observation window, leads to a circular field of view with a diameter of about 5.6 mm (Fig. 1a). Radiographs were captured at a scan rate of 50 half-frames per second, then integrated over a period of 1 s.

The analysis of the solidification front velocity, plume, tip growth, and primary dendritic arm spacing followed the algorithm proposed by Boden *et al.*<sup>18</sup> The concentration profiles were determined from measurements of the local brightness in the images. Composition calibrations were performed by using reference measurements in cells filled with pure liquid Ga and with the Ga-25 wt%In alloy.

## NUMERICAL METHOD

The bespoke numerical code Thermo Electric Solidification Algorithm (TESA) used in this work couples the governing equations for solidification,

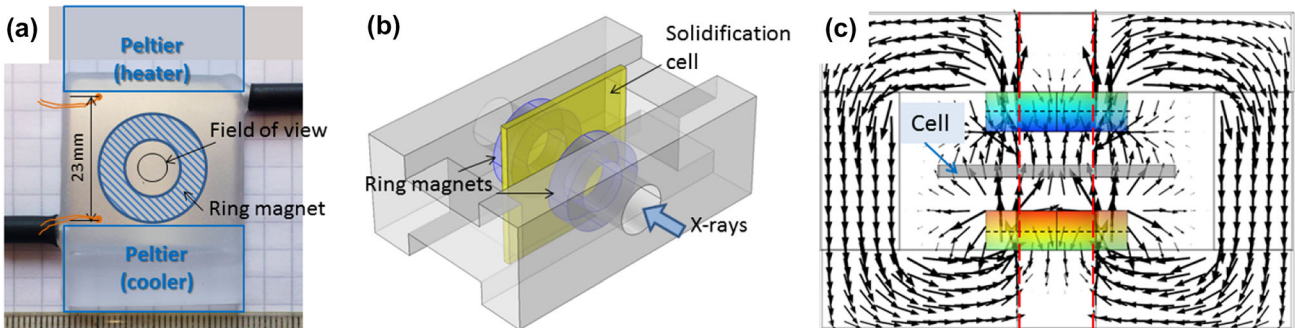


Fig. 1. Experimental setup with magnetic field: (a) schematic view of solidification cell aligned to X-ray source, (b) isometric view, and (c) top-down view with calculated magnetic field lines.

fluid flow, electromagnetism, and transport of heat and mass. Transient phase change and the partitioning of solute are given by

$$C_l(1-k)\frac{\partial\phi_s}{\partial t} = -\nabla \cdot (D_e\nabla C_l) + [1 - (1-k)\phi_s]\frac{\partial C_l}{\partial t} \quad (1)$$

where  $C_l$  is the liquid concentration,  $k$  is the partitioning coefficient,  $D_e$  is the mass diffusivity, and  $\phi_s$  is the volume solid fraction. Mass transport in terms of concentration is given by

$$\frac{\partial C_e}{\partial t} + \mathbf{u} \cdot \nabla C_l = \nabla \cdot (D_e\nabla C_l), \quad (2)$$

where  $C_e = (1 - \phi_s)C_l + \phi_s C_s$ ,  $\mathbf{u}$  is the fluid velocity, and  $C_s$  is the concentration in the solid. The current density,  $\mathbf{j}$ , comes from a generalized form of Ohm's law that includes the thermoelectric field, given by

$$\mathbf{j} = \sigma(\mathbf{E} - S\nabla T + \mathbf{u} \times \mathbf{B}) \quad (3)$$

where  $\sigma$  is the electrical conductivity,  $\mathbf{E}$  is the electric field,  $S$  is the Seebeck coefficient,  $\nabla T$  is the thermal gradient, and  $\mathbf{B}$  is the magnetic field. The fluid flow is governed by the Navier–Stokes equations, given by

$$\frac{\partial \mathbf{u}}{\partial t} + \mathbf{u} \cdot \nabla \mathbf{u} = -\frac{1}{\rho}\nabla p + \nu\nabla^2 \mathbf{u} + \mathbf{F}, \quad (4)$$

where  $\rho$  is the reference density,  $p$  is the pressure,  $\nu$  is the kinematic viscosity, and  $\mathbf{F}$  is the sum of body forces acting on the fluid, namely the Lorentz force,  $\mathbf{j} \times \mathbf{B}$ , and solutal buoyancy forces giving

$$\mathbf{F} = \mathbf{j} \times \mathbf{B} + \rho\mathbf{g}(\beta_C(C_l - C_0)), \quad (5)$$

where  $\mathbf{g}$  is the acceleration due to gravity,  $\beta_C$  is the solutal expansion coefficient, and  $C_0$  is a reference concentration set to bulk conditions.

TESA consists of four key solvers: a cellular automata (CA) method for solidification<sup>19</sup> based on the  $\mu$ MatIC code,<sup>20–23</sup> a lattice Boltzmann method<sup>24</sup> for hydrodynamics, and finite difference methods for electromagnetism and the transport equations. TESA<sup>25,26</sup> has been validated and applied to various similar systems, including a study of channel formation in Ga-25 wt%In alloy.<sup>14</sup> The computational domain is on the scale of the entire experiment, using  $3200 \times 16 \times 3200$  cubic cells with length of  $10 \mu\text{m}$ . The boundaries of the domain represent walls with zero velocity and no mass flux, except for the far-field boundary at the top, which is set to fixed pressure and bulk concentration values. In all the numerical cases,  $\nabla T = 2 \text{ K/mm}$  and the cooling rate is  $0.01 \text{ K/s}$ . The base of the domain is nucleated with 20 equally spaced seeds with growth orientations aligned along the thermal gradient. This idealized grain

structure was selected as the growth orientation has been shown to influence plume formation<sup>23</sup> and may dominate over TEMHD-based mechanisms (Table 1).

## RESULTS

Using the ring magnet system described above, experiments were conducted on a thin sample of Ga-25 wt%In alloy with *in situ* X-ray radiography imaging. In contrast to experiments in the absence of a magnetic field, the application of the magnetic field introduced significant microstructural changes. The main feature is preferential growth of secondary arms, caused by TEMHD interdendritic flow. In this case, the flow due to TEMHD in the mushy zone is from right to left, sweeping concentration downstream and creating a growth bias of the secondary arms. A second feature is a modification to the primary arm spacing that has been observed in *ex situ* experiments<sup>11</sup> and can also be attributed to the TEMHD effect. A comparison of the experimental microstructures with and without a magnetic field is shown in Fig. 2. Figure 2a shows the symmetric secondary growth without a magnetic field, while Fig. 2b, c shows preferential growth under a magnetic field, highlighting that TEMHD effects can be observed with differing solidification conditions, in this case cooling rate, hence growth velocity.

The *in situ* experiments also revealed an additional phenomenon ahead of the interface, with the lateral migration of the escaping plumes to the left side of the sample. Since buoyancy only acts in the vertical direction, an initial analysis of these results indicated that a pressure bias introduced by TEMHD flow was the primary mechanism underlying the observed phenomenon.<sup>17</sup>

To provide a clearer explanation of the overall mechanism, TESA was configured to simulate the experimental parameters. Figure 3a, b shows good agreement between the experimental and numerical results, highlighting that plume migration and preferential secondary arm growth are also captured by the numerical model.

The thermoelectric currents generally form circulations between the solid and liquid, with a dominant component along the thermal gradient. In this case, Fig. 3c shows current flowing up in the liquid and down in the solid, and with the magnetic field normal to the plane of the sample, the TEF in the liquid points to the left of the sample, driving fluid flow from the right to left, while in the solid the TEF is balanced by elastic structural forces. This leads to transverse flow through the dendritic network, shown in Fig. 3d, which causes preferential growth and macrosegregation. The latter leads to the formation of a stable channel on the side of the sample, fed by TEMHD. A continuous high-velocity stream of high-concentration fluid emanates from the channel, shown in Fig. 3e; this in turn

**Table 1. Material property values used for simulation**

Property	Variable	Value	Unit
Reference density	$\rho$	6326	$\text{kg m}^{-3}$
Reference concentration	$C_0$	75	
Kinematic viscosity	$\nu$	$3.28 \times 10^{-7}$	$\text{m}^2\text{s}^{-1}$
Partitioning coefficient	$k$	0.5	–
Solute diffusivity	$D_l$	$2 \times 10^{-9}$	$\text{m}^2\text{s}^{-1}$
Liquidus slope	$m_l$	2.9	$\text{K wt}\%^{-1}$
Solute expansion coefficient	$\beta_C$	$1.66 \times 10^{-3}$	$\text{wt}\%^{-1}$
Thermal expansion coefficient	$\beta_T$	$1.18 \times 10^{-4}$	$\text{K}^{-1}$
Electrical conductivity	$\sigma$	$3.6 \times 10^6$	$\text{S m}^{-1}$
Seebeck power	$\Delta S$	$8 \times 10^{-7}$	$\text{V K}^{-1}$

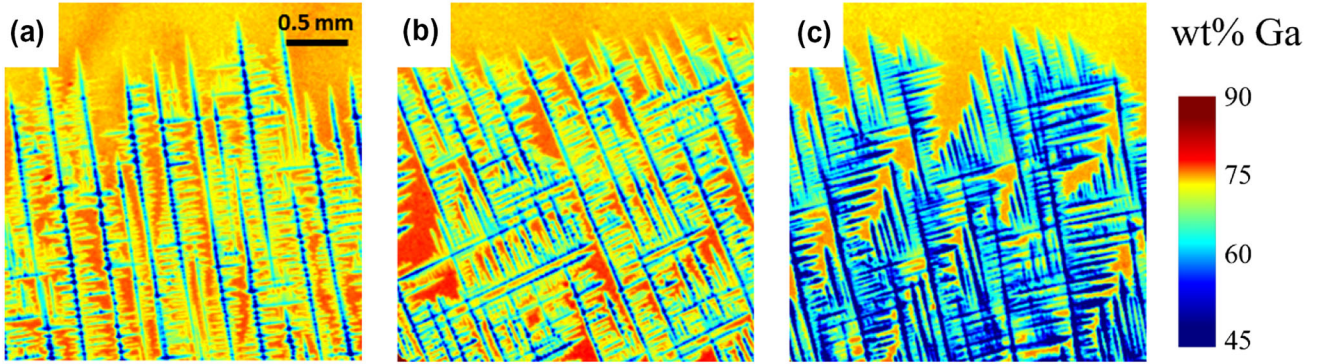


Fig. 2. Morphology of dendritic structure of directionally solidified Ga-25 wt%In alloy at temperature gradient of 2 K/mm with and without the transverse magnetic field: (a) 0.01 K/s, 0 T; (b) 0.01 K/s, 0.19 T; (c) 0.005 K/s, 0.19 T.

introduces a suction force that manifests as a low-pressure region that extends from the mouth of the channel ahead of the interface as shown in Fig. 3e. This pressure drop not only sucks fluid from inside the channel, but also generates a lateral pressure gradient ahead of the interface, driving a cross flow, and it is this flow which, as predicted by the model, is the main driver of plume migration. Figure 3d shows the strong lateral flow ahead of the interface.

The ring magnets used to apply the external field obscure the field of view in the experiments, preventing a direct comparison with the simulations in the vicinity of the sample walls. Nevertheless, the numerical results also reveal the mechanism for the initiation of plume migration. During the initial solidification of the first 4 mm of the sample, there was no strong evidence of lateral plume migration, although the influence of TEMHD on the microstructure is still evident. This can be seen in Fig. 4a, where both preferential growth of the secondary arms and the formation of a macrosegregation region can be seen. However, towards the bulk, high concentration plumes are relatively evenly distributed across the top of the domain. Once the interface had grown to 8 mm, the migration of plumes became evident and can be seen in Fig. 4b, where the high-concentration regions in the bulk have shifted to the left side of the sample. This

contrasts with Fig. 4c, which shows the growth with no magnetic field at a height of 10 mm but exhibits similar behavior to the results in Fig. 4a. The plume migration behavior therefore cannot be explained by the influence of TEMHD alone, as the volumetric TEF would be similar at both interface heights. Furthermore, the current density is localized to the mushy zone, thus the TEF is also localized and diminishes far from the interface as shown in Fig. 3c. However, the initiation of the plume migration coincided with the formation of a stable channel on the left side of the sample. After this had formed, the plumes continuously migrated across the interface as a consequence of continuity.

To summarize, plume migration is caused by macrosegregation at the sample wall from TEMHD, which in turn forms a stable channel that then creates a suction force across the interface. This also explains why there is a delay in the numerical model before the onset of plume migration. There is a critical interface height for a stable channel to form,<sup>3,4,14,27</sup> which is a consequence of the required mass flux from the interdendritic region feeding the mass flux exiting the channel. As the interface height increases through solidification, the cross-sectional area of the interdendritic region increases until TEMHD flow can sustain a stable channel.

Magnetic Effects on Microstructure and Solute Plume Dynamics of Directionally Solidifying Ga-In Alloy

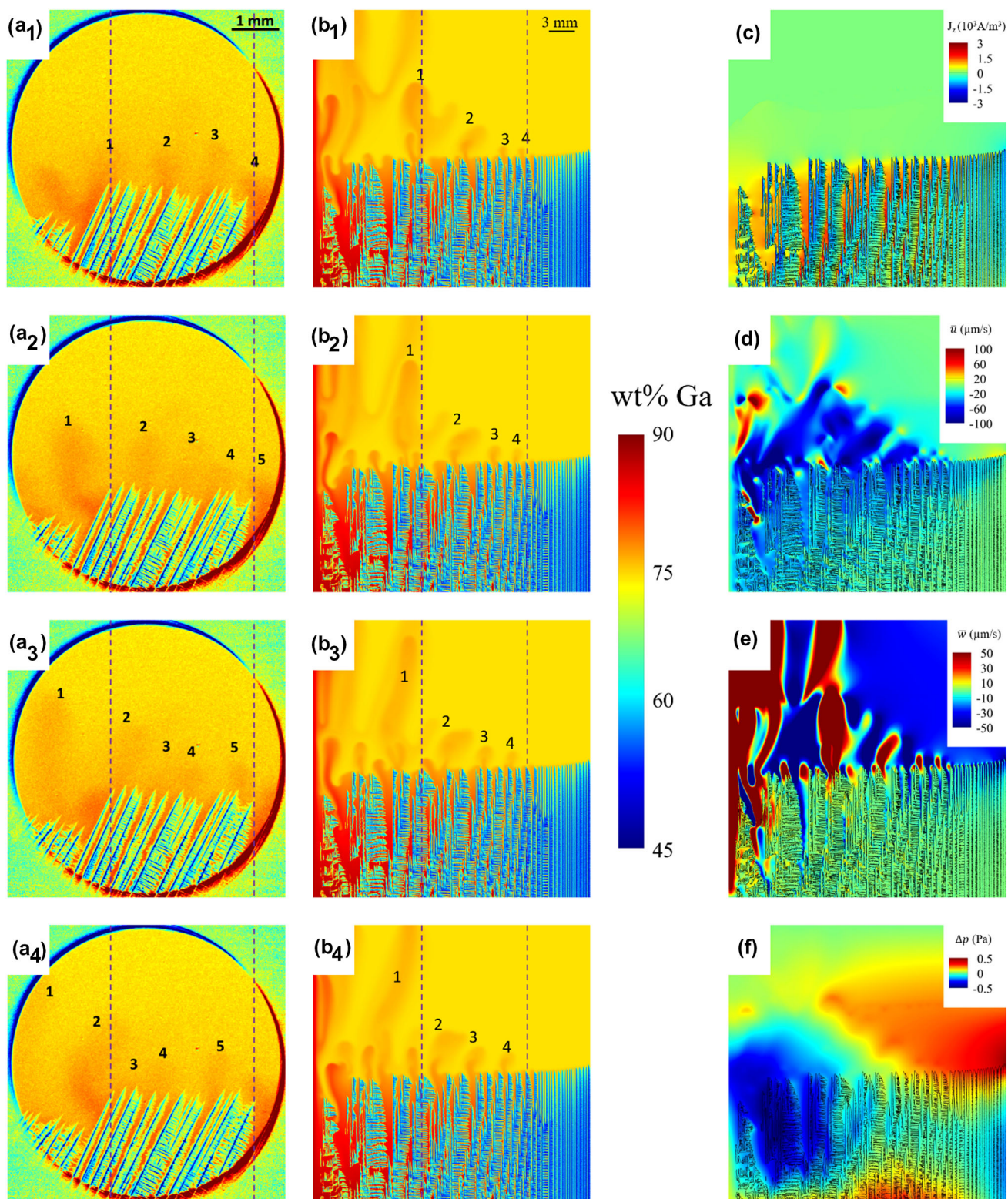


Fig. 3. Comparison of experiments (a) with numerical calculations (b); individual plumes are numbered and tracked in time at 25-s increments. (a<sub>1</sub>–a<sub>4</sub>) Experimental transient migration of plumes. (b<sub>1</sub>–b<sub>4</sub>) Numerical transient migration of plumes. (c) Current density. (d) Average x-component of velocity. (e) Average z-component of velocity. (f) Relative pressure.

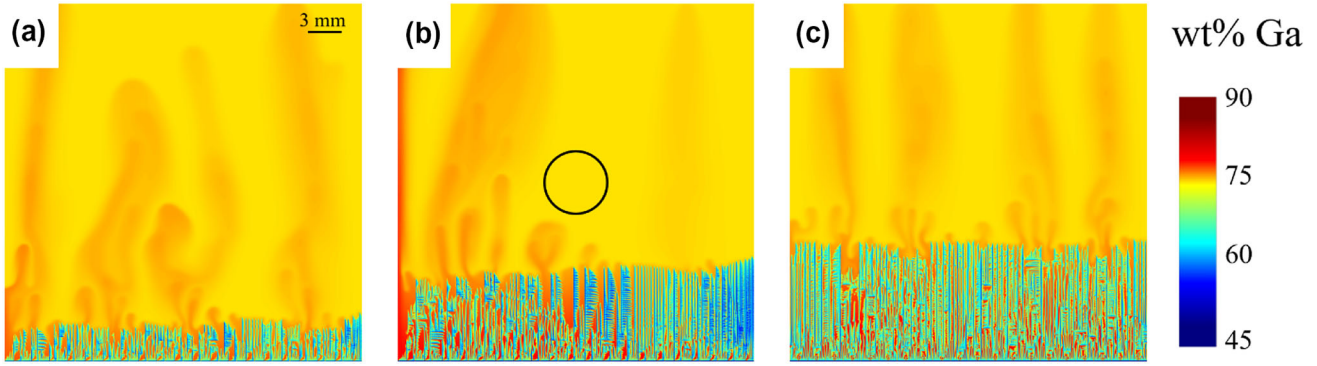


Fig. 4. Simulation of early stages of growth with and without magnetic field: (a) 4 mm growth and  $|B| = 0.2$  T, (b) 8 mm growth and  $|B| = 0.2$  T (circle indicates experimental FOV), and (c) 10 mm growth and  $|B| = 0$ .

The model also predicts significant microstructural changes. As discussed above, preferential growth of the secondary arms due to incident TEMHD flow was observed in the experiments and predicted in the model. The model shows that, in the downstream direction, toward the channel, there is significant remelting and regrowth, and the formation of large pockets of high-concentration liquid. Such pockets have been observed experimentally with the application of a magnetic field.<sup>6,9</sup> Upstream, on the right side of the sample, bulk flow is incident to the interface to preserve continuity of mass from TEMHD driving interdendritic flow. This flow encourages growth, causing coarsening as the low-concentration liquid passes through the interdendritic network. This can be seen in the results as a low-concentration region of tightly packed dendrites in Fig. 3b. The primary arm spacing varies across the domain from the smallest on the right side with incident bulk flow and increasing toward the left side with the channel. These predictions are consistent with *ex situ* findings in literature,<sup>11</sup> but this work highlights how capturing the *in situ* dynamics both experimentally and computationally can reveal the underlying dynamics.

## CONCLUSION

The effects of applying a 0.2-T transverse magnetic field to a solidifying Ga-25 wt%In alloy were investigated through a joint experimental and numerical study. The magnetic field introduced several significant changes to both the microstructure and the dynamics of escaping high-concentration Ga plumes. The microstructure exhibited preferential growth of the secondary arms, modification to the primary arm spacing, coarsening on one side of the sample, and the formation of pockets or bands through remelting and resolidification on the other. These effects can all be attributed to TEMHD flow. TEMHD also introduced macrosegregation that led to the formation of a

stable channel downstream of the flow. This in turn was shown to introduce a secondary hydrodynamic phenomenon that led to the migration of plumes across the interface. Some of these phenomena could not be directly observed as they were obscured by the magnetic rig. However, an excellent match between the experimental observations and numerical predictions was found in the region where observations could be taken. This gives a high confidence in the predictive power of the model presented, opening new avenues of investigation on how magnetic fields can be used to beneficially control the microstructural evolution of related alloys such as nickel-based superalloys. Further investigation, to apply a magnetic field without obscuring the field of view of the sample, would be a worthwhile exercise, to capture both the microscopic and macroscopic dynamics.

Although the magnetic field was relatively homogeneous in the center of the sample, there are larger variations towards the edges and outside the outer diameter of the magnet. These magnetic field variations would lead to a spatial variation in the Lorentz force within the mushy zone. This would lead to variations in pressure gradient to balance this force, but with the Lorentz force still oriented in the same direction there would still be a net transport of solute as predicted by the current simulations. To obtain a better match between the experimental and numerical results, these magnetic field variations could also be included in future work.

The primary arm spacing in the model is larger than those in the experiments and may be a consequence of the idealized orientation used. It is not immediately clear whether this is a numerical artifact. Numerical methods can suffer from grid anisotropy, which could explain this, however with the dendrites orientated along the thermal gradient, the flow effect of preferential secondary growth would also be at a maximum. Thus, a competition between primary arms and secondary arms would take place and, with conditions favorable for

secondaries, would lead to an effective increase in the primary arm spacing. Therefore, there are still many interesting avenues to explore for investigating the combined interaction of grain orientation, TEMHD, and channel formation.

### ACKNOWLEDGEMENTS

Part of this study was funded by the UK Engineering and Physical Sciences Research Council (EPSRC) under grant EP/K011413/1. In this work, S.H. was funded by the Natural Science Foundation of China (Nos. 51690162, 51701112, 51604171), National Science and Technology Major Project (No. 2017-VII-0008-0102), and China Scholarship Council (No. 201806890052). P.D.L. acknowledges support from the Royal Academy of Engineering (CiET1819/10) and EPSRC (EP/P006566).

### CONFLICT OF INTEREST

On behalf of all authors, the corresponding author states that there are no conflicts of interest.

### OPEN ACCESS

This article is licensed under a Creative Commons Attribution 4.0 International License, which permits use, sharing, adaptation, distribution and reproduction in any medium or format, as long as you give appropriate credit to the original author(s) and the source, provide a link to the Creative Commons licence, and indicate if changes were made. The images or other third party material in this article are included in the article's Creative Commons licence, unless indicated otherwise in a credit line to the material. If material is not included in the article's Creative Commons licence and your intended use is not permitted by statutory regulation or exceeds the permitted use, you will need to obtain permission directly from the copyright holder. To view a copy of this licence, visit <http://creativecommons.org/licenses/by/4.0/>.

### REFERENCES

1. R.C. Reed, T. Tao, and N. Warnken, *Acta Mater.* 57, 5898 (2009). <https://doi.org/10.1016/j.actamat.2009.08.018>.
2. J.D. Madison, Ph.D. Thesis, University of Michigan (2010) <hdl.handle.net/2027.42/76001>.
3. P. Auburtin, T. Wang, S.L. Cockcroft, and A. Mitchell, *Metall. Mater. Trans. B* 31, 801 (2000). <https://doi.org/10.1007/s11663-000-0117-9>.
4. C. Beckermann, J.P. Gu, and W.J. Boettinger, *Metall. Mater. Trans. A* 31, 2545 (2000). <https://doi.org/10.1007/s11661-000-0199-7>.
5. J. Wang, Z. Ren, Y. Fautrelle, X. Li, H. Nguyen-Thi, N. Mangelinck-Noel, G.S.A. Jaoude, Y. Zhong, I. Kaldre, and A.

6. Bojarevics, *J. Mater. Sci.* 48, 213 (2013). <https://doi.org/10.1007/s10853-012-6730-6>.
6. S.N. Tewari, R. Shah, and H. Song, *Metall. Mater. Trans. A* 25, 1535 (1994). <https://doi.org/10.1007/BF02665485>.
7. P. Lehmann, R. Moreau, D. Camel, and R. Bolcato, *Acta Mater.* 46, 4067 (1998). [https://doi.org/10.1016/S1359-6454\(98\)00064-0](https://doi.org/10.1016/S1359-6454(98)00064-0).
8. X. Li, D. Du, A. Gagnoud, Z. Ren, Y. Fautrelle, and R. Moreau, *Metall. Mater. Trans. A* 45, 5584 (2014). <https://doi.org/10.1007/s11661-014-2496-6>.
9. X. Li, Y. Fautrelle, Z. Ren, and R. Moreau, *Sci. Rep.* 7, 45834 (2017). <https://doi.org/10.1038/srep45834>.
10. Z.Y. Lu, Y. Fautrelle, and X. Li, *Metall. Mater. Trans. A* 49, 4383 (2018). <https://doi.org/10.1007/s11661-018-4604-5>.
11. X. Li, Z. Ren, J. Wang, Y. Han, and B. Sun, *Mater. Lett.* 67, 205 (2012). <https://doi.org/10.1016/j.matlet.2011.07.031>.
12. W. Xuan, H. Liu, J. Lan, C. Li, Y. Zhong, X. Li, G. Cao, and Z. Ren, *Metall. Mater. Trans. A* 47, 3231 (2016). <https://doi.org/10.1007/s11663-016-0790-y>.
13. X. Li, J. Wang, J. Zhang, Y. Han, and X. Li, *Materials* 8, 3428 (2015). <https://doi.org/10.3390/ma8063428>.
14. A. Kao, N. Shevchenko, M. Alexandrakis, I. Krastins, S. Eckert, and K. Pericleous, *Phil. Trans. R. Soc. A* 377, 20180206 (2019). <https://doi.org/10.1098/rsta.2018.0206>.
15. N. Shevchenko, O. Roshchupkina, O. Sokolova, and S. Eckert, *J. Cryst. Growth* 417, 1 (2015). <https://doi.org/10.1016/j.jcrysgro.2014.11.043>.
16. N. Shevchenko, S. Boden, G. Gerbeth, and S. Eckert, *Metall. Mater. Trans. A* 44, 3797 (2013). <https://doi.org/10.1007/s11661-013-1711-1>.
17. S. He, N. Shevchenko, and S. Eckert, *IOP Conference Series: Materials Science and Engineering MCWASP XV: International Conference on Modelling of Casting, Welding and Advanced Solidification Processes*, in press.
18. S. Boden, B. Willers, S. Eckert, and G. Gerbeth, *Metall. Mater. Trans. A* 39, 613 (2008). <https://doi.org/10.1007/s11661-007-9462-5>.
19. M. Alexandrakis, Ph.D. Thesis, University of Greenwich (2018).
20. W. Wang, P. Lee, and M. McLean, *Acta Mater.* 51, 2971 (2003). [https://doi.org/10.1016/s1359-6454\(03\)00110-1](https://doi.org/10.1016/s1359-6454(03)00110-1).
21. L. Yuan and P.D. Lee, *Modell. Simul. Mater. Sci. Eng.* 18, 055008 (2010). <https://doi.org/10.1088/0965-0393/18/5/055008>.
22. L. Yuan and P.D. Lee, *Acta Mater.* 60, 4917 (2012). <https://doi.org/10.1016/j.actamat.2012.04.043>.
23. S. Karagadde, L. Yuan, N. Shevchenko, S. Eckert, and P.D. Lee, *Acta Mater.* 79, 168 (2014). <https://doi.org/10.1016/j.actamat.2014.07.002>.
24. I. Krastins, A. Kao, K. Pericleous, and T. Reis, *Int. J. Numer. Methods Fluids* (2020). <https://doi.org/10.1002/flid.4856>.
25. A. Kao, I. Krastins, M. Alexandrakis, N. Shevchenko, S. Eckert, and K. Pericleous, *JOM* 71, 48 (2019). <https://doi.org/10.1007/s11837-018-3195-3>.
26. A. Kao, T. Gan, C. Tonry, I. Krastins, and K. Pericleous, *Phil. Trans. R. Soc. A* 378, 20190249 (2020). <https://doi.org/10.1098/rsta.2019.0249>.
27. S.D. Felicelli, J.C. Heinrich, and D.R. Poirier, *Int. J. Numer. Meth. Fluids* 27, 207 (1998). [https://doi.org/10.1002/\(SICI\)1097-0363\(199801\)27:1/4%3C207::AID-FLD660%3E3.0.CO;2-X](https://doi.org/10.1002/(SICI)1097-0363(199801)27:1/4%3C207::AID-FLD660%3E3.0.CO;2-X).

**Publisher's Note** Springer Nature remains neutral with regard to jurisdictional claims in published maps and institutional affiliations.